Semiquantum vs. quantum methods for grazing-incidence fast atom diffraction: influence of the wave-packet size

A. S. Muzas,[1,*] L. Frisco,[2,*] G. A. Bocan,[3] C. Díaz,[4] and M. S. Gravielle[2,†]

[1] *Departamento de Química Física Aplicada, Universidad Autónoma de Madrid, 28049 Madrid, Spain*
[2] *Instituto de Astronomía y Física del Espacio (UBA-CONICET), Ciudad Universitaria, (C1428EGA) Buenos Aires, Argentina*
[3] *Instituto de Nanociencia y Nanotecnología, Nodo Bariloche (CONICET-CNEA) and Instituto Balseiro (U. N. Cuyo), Centro Atómico Bariloche, Avenida Bustillo 9500, 8400 San Carlos de Bariloche, Argentina*
[4] *Departamento de Química Física, Facultad de CC. Químicas, Universidad Complutense de Madrid, 28040 Madrid, Spain*

(Dated: March 1, 2024)

To take full advantage of the capabilities of grazing incidence fast atom diffraction (GIFAD) as an experimental technique for analyzing surfaces and phenomena that occur on them, versatile theoretical tools are needed that accurately describe the experiments while allowing a simple but meaningful interpretation at a reasonable computational cost. During the last years, the semiquantum method named surface initial value representation (SIVR) has been postulated to fill this room. However, to date, SIRV has not yet been validated using full quantum calculations as a reference. Here, we have contrasted GIFAD simulations performed with the SIVR approach with those obtained with the full quantum method known as Multi Configuration Time Dependent Hartree (MCTDH), taking into account the influence of the size of the initial wave packet. Our comparative study, using GIFAD for the He-LiF(001) system as a benchmark, shows a very good agreement, both qualitative and quantitative, between SIVR and MCTDH simulated diffraction spectra, under different incidence conditions. These findings support the use of SIVR as a versatile theoretical tool to extract as much accurate information as possible from GIFAD experiments.

I. INTRODUCTION

The grazing incidence fast atom diffraction (GIFAD) experimental technique [1, 2] is a very promising surface analysis tool [3, 4], which could be used both as a complement and as an alternative to well-known and widely used thermal-energy atom scattering (TEAS) [5–8] and reflection high energy electron diffraction (RHEED) [9, 10]. However, to extract as much information as possible from GIFAD measurements it is essential to have reliable theoretical tools able to accurately simulate and describe such experiments. Available theoretical methods to describe GIFAD range from purely classical to semiclassical and semiquantum to purely quantum methods [11]. All of them are based on the validity of the Born-Oppenheimer approximation, which allows one to disentangle the electronic structure calculation from that of the nuclei dynamics. Regarding the electronic structure, we can find in the literature a handful of methods, relying on the use of density functional theory (DFT) and periodic boundary conditions (PBC), that yield accurate potential energy surfaces (PES) [12–16]. In this study, we have used the corrugation reducing procedure (CRP) [16] to build our PES. Regarding the nuclei dynamics, pure classical methods allow one to obtain some physical insights by analyzing the classical trajectories, at a very low computational cost (see, e.g., GIFAD classical results for H/LiF(001) [17]), but they lack a suitable description of the quantum mechanisms involved in GIFAD. Pure quantum GIFAD simulations, on the other hand, accurately capture the physics associated with interference phenomena [18–20], but at the price of much higher complexity and computational cost, and a less intuitive physical interpretation. A compromise between these two extreme methods is the use of semiclassical or semiquantum methods, which satisfactorily describe quantum phenomena while keeping the simplicity of a classical analysis.

A semiclassical method was in fact used to theoretically predict GIFAD five years before it was experimentally observed [21]. Since then, different flavors of semiclassical dynamics have been used, aiming to unravel the main physical mechanisms that underlie this phenomenon. Among them, the simplest ones are those based on three-dimensional (3D) classical trajectories that combine classical [22–26] or local classical [27] scattering cross sections incorporating a phase to account for the quantum interference, and those based on the surface eikonal approximation [28–32]. These methods provide, in general, a good representation of the experimental diffraction patterns, but largely overestimate the intensity of the outermost maxima of the angular distribution which are close to the classical rainbow angles. Noteworthy, the surface initial value representation (SIVR) approximation [33] is a semiquantum method which solves this shortcoming. SIVR takes into account the quantum effects associated with GIFAD, such as classically forbidden transitions, interference, and coherence lengths, without losing the appealing representation of the interference mechanisms in terms of classical tra-

*These authors contributed equally
†Electronic address: msilvia@iafe.uba.ar

jectories. The SIVR approach, including its extension phonon-SIVR [34] that incorporates phonon transitions, has already been used to describe several GIFAD experiments [33, 35–40]. However, it has never been tested using full-dimensional quantum computations as a reference. Such a comparison would allow us to study the validity limit of this approximation.

With this idea in mind, in this article we compare semiquantum SIVR and pure quantum Multi Configuration Time Dependent Hartree (MCTDH) calculations [41, 42] for He/LiF(001) GIFAD along the ⟨110⟩ channel, using the same PES and the same initial conditions. For this test, it is necessary to take into account that, as in the experiments [43], within the SIVR approach the collimating scheme governs the transverse coherence length of the incident wave packet, which determines the azimuthal width of the diffraction peaks. In contrast, the MCTDH method considers the incidence of an ideal extended plane wave on the surface plane, and, consequently, the interference maxima become perfect delta functions located at the Bragg angles. Therefore, in order to enable the MCTDH-SIVR comparison, we analyze the influence of the profile of the incident wave function on the MCTDH patterns by considering Gaussian wave packets with different transverse widths. Concerning the SIVR method, although the incident projectile is always described as a wave packet, different bases of intermediate quantum states, ranging from position to momentum eigenstates, can be used to derive the IVR time-evolution operator [44], which is the kernel of the SIVR approximation. Since one of the most common intermediate bases employed within the IVR description corresponds to Gaussian wave packets with fixed spatial and momentum widths, in this work we use these intermediate states to study the dependence of the SIVR results on the choice of the intermediate basis. Our study highlights the remarkable agreement, both qualitative and quantitative, between MCTDH and SIVR results, when the transverse width of the intermediate states coincides with that of the initial wave packet. Thus, these findings validate the use of this latter semiquantum approach to study phenomena associated with GIFAD.

In this article, atomic units (a.u.) are used unless otherwise stated.

II. THEORETICAL MODELS

A. Projectile-surface potential

The He-LiF(001) PES is built by combining PBC-DFT calculations, performed with the planewaves-based package QUANTUM ESPRESSO [45], with a multidimensional interpolation technique, involving cubic splines and the CRP procedure [16].

Within the DFT calculations, the electron-core interactions are described with projector augmented-wave (PAW) pseudopotentials [46, 47], while the Perdew-Burke-Ernzerhof (PBE) functional [48] is used to account for exchange-correlation within the generalized gradient approximation (GGA). The optimization of the LiF bulk geometry yields a lattice constant of 7.684 a.u. (4.066 Å), in good agreement with the experimental value, 4.02 Å[49].

We represent the LiF(001) surface by means of the supercell-slab scheme. The supercell consists of a $\sqrt{2} \times \sqrt{2}$ surface cell, a six-layer slab, and a vacuum layer of $\sim$ 14.23 Å. The relaxed surface equilibrium geometry presents a rumpling, defined as the half-distance between relaxed F and Li planes. For the topmost F and Li planes, we get a rumpling of +0.036 Å, with F atoms moving outward and Li atoms moving inward. This value is consistent with previous works [50] and with LEED experiments which yield a rumpling of 0.02 ± 0.01Å [49].

We make use of PBC-DFT calculations to evaluate the potential energy of the He-LiF(001) system over a three-dimensional grid of He-atom positions (X_i, Y_i, Z_i), where Z_i is the coordinate in the direction normal to the LiF(001) surface. We consider 6 high-symmetry (X_i, Y_i) configurations and 28 non-equidistant Z_i values between 0.13 Å and 6.88 Å. In the calculations, the energy cutoff in the plane-wave expansion has been set on 80 Ryd for the wave functions and 480 Ryd for the charge density and potential. A $2\times2\times1$ Monkhorst–Pack grid of special k-points (shifted from the origin in the directions parallel to the surface) is used for the Brioullin-zone integration. With this choice of parameters, ab initio energies are converged within 1 meV.

B. Quantum simulations: MCTDH method

The MCTDH method [41, 51] allows one to efficiently compute quantum probabilities for projectile/surface systems, as previously shown for both molecular reactivity [52–54] and atomic diffraction [55, 56]. Within the MCTDH framework, we solve the time-dependent Schrödinger equation,

$$\hat{H}\Psi(\mathbf{R},t) = i\frac{\partial\Psi(\mathbf{R},t)}{\partial t}, \tag{1}$$

by representing the time-dependent nuclear wave function of the atomic projectile $\Psi(\mathbf{R},t)$ as a sum of Hartree products of time-dependent single-particle functions (SPFs), such as:

$$\Psi(q_1,q_2,q_3,t) = \sum_{i_1=1}^{m_1}\sum_{i_2=1}^{m_2}\sum_{i_3=1}^{m_3} A_{i_1,i_2,i_3}(t)\prod_{k=1}^{3}\phi_{i_k}^{(k)}(q_k,t). \tag{2}$$

In this equation, q_k represents the k^{th} mode, which in our particular case is equal to the k^{th} degree of freedom of the projectile, and $A_{i_1,i_2,i_3}(t)$ are the time-dependent expansion coefficients. The SPFs ($\phi_{i_k}^{(k)}$), on the other

hand, are expanded in a primitive time-independent basis set, such as:

$$\phi_{i_k}^{(k)}(q_k,t) = \sum_{j_k=1}^{N_k} a_{j_k,i_k}^{(k)} \chi_{j_k}^{(k)}(q_k). \tag{3}$$

Within this formalism, the equations of motion for both the SPFs and the expansion coefficients are derived from the Dirac-Frenkel variational principle, leading to a set of coupled equations. At this point, it should be noticed that the efficiency of the MCTDH algorithm can be improved by expressing the potential as a sum of one-dimensional (1D) functions. Thus, we have transformed our non-separable PES corresponding to the 3D projectile-surface interaction ($V_{PS} \equiv V^{3D}$) into this form by employing the so-called POTFIT algorithm [57, 58], which approximates the potential as:

$$V^{3D} \approx V^{app} = \sum_{i_1=1}^{m_1} \sum_{i_2=1}^{m_2} \sum_{i_1=3}^{m_3} C_{i_1,i_2,i_3} v_{i_1}(q_1) v_{i_2}(q_2) v_{i_3}(q_3), \tag{4}$$

where v_{i_k} are 1D natural potentials and C_{i_1,i_2,i_3} are the expansion coefficients, which are calculated as the overlaps between the non-separable PES and the natural potentials. To ensure accuracy of V^{app}, one can perform an iteration process to improve the potential description inside the relevant dynamical region. To do so, a modified reference potential $\hat{V}^{3D}$ is defined as a linear combination of the exact and fitted potentials, such as:

$$\hat{V}^{3D}_{i_1 i_2 i_3} = w_{i_1 i_2 i_3} V^{3D}_{i_1 i_2 i_3} + (1 - w_{i_1 i_2 i_3}) V^{app}_{i_1 i_2 i_3} \tag{5}$$

In this equation, the weight function (w) is set to 1 inside the relevant dynamical region, and < 1 outside this region. To optimize the interaction process, avoiding numerical inaccuracies in the potential fitting of the repulsive regions, a maximum potential value is set up during the procedure.

Finally, a flux analysis of the reflected wave function is performed to obtain diffraction probabilities, upon absorption by a complex absorbing potential, $W_{Z_0} = \eta_z (Z - Z_0)^n \theta(Z - Z_0)$, which is placed in the non-interacting vacuum region. The MCTDH probabilities shown throughout this article have been obtained using the Heidelberg MCTDH package [59]. In Appendix B (Table II), we have listed the parameters used in the calculations.

1. *Dependence on the initial wave function*

In MCTDH simulations, the result of the flux analysis will depend on the form of the initial wave function. One option is to perform *full* coherence (perfect collimation) calculations by using an initial wave function written as a product of a Gaussian function in the direction perpendicular to the surface (z direction) and a plane wave in the surface plane (x and y directions), such as:

$$\Psi(\mathbf{R}, t_0) \propto \mathrm{e}^{-(\frac{Z-Z_0}{\sigma_z})^2} \mathrm{e}^{i\mathbf{K}_i \cdot (\mathbf{R}-\mathbf{R}_0)}. \tag{6}$$

where $\mathbf{R}_0 = (X_0, Y_0, Z_0)$ is the mean projectile position at the initial time t_0, with Z_0 placed in the non-interacting region far from the surface, σ_z is twice the standard deviation of the probability distribution of the wave packet in Z direction, and $\mathbf{K}_i$ is the initial projectile momentum.

In this first case, we describe the diffraction of a projectile that has a very precise initial momentum parallel to the surface plane from an infinite periodic crystal, which is associated with the *full* coherence condition. Hence, the diffraction spectra present Bragg peaks that are perfect delta functions placed on the Laue circle $\theta_f^2 + \varphi_f^2 = \theta_i^2$, where θ_f (θ_i) is the final (initial) polar angle, measured with respect to the surface, and φ_f is the final azimuthal angle measured with respect to the axial channel (x direction). The intensities of the Bragg peaks are governed by intrachannel interference, i.e., inside a unique channel (see the inset of Fig. 1), a.k.a. form factor. Such intrachannel interference gives rise to rainbow and supernumerary rainbow maxima that modulate the heights of the delta functions. On the other hand, their azimuthal positions, $\varphi_f^{(B)}$, are determined by interchannel interference (a.k.a. structure factor), reading $\varphi_f^{(B)} = \arcsin(n\lambda/d_y)$, where $\lambda = 2\pi/K_i$ is the de Broglie wavelength of the incident projectile, d_y is the width of the channel, and n (integer number) is the Bragg order [25].

Another option is to take into account collimation effects by considering a finite transverse coherence length σ_y in the initial wave function [35, 43]. To do so, we introduce a Gaussian function to describe the motion along the y direction, perpendicular to the incidence direction, such as:

$$\Psi(\mathbf{R}, t_0) \propto \mathrm{e}^{-(\frac{Z-Z_0}{\sigma_z})^2} \mathrm{e}^{-(\frac{Y-Y_0}{\sigma_y})^2} \mathrm{e}^{i\mathbf{K}_i \cdot (\mathbf{R}-\mathbf{R}_0)}. \tag{7}$$

In this second case, the initial wave packet is centered at (Y_0, Z_0) with associated transverse widths σ_y and σ_z and uniformly delocalised along the x axis, that is, a combination of a plane wave and Gaussian wave packets. As a result, the azimuthal spectrum presents non-zero diffraction probabilities outside the Bragg positions $\varphi_f^{(B)}$, which yields diffraction peaks with a characteristic width. Now, the computation of such diffractograms requires a flux analysis in a uniformly distributed ensemble of initial wave packets in the y axis and a grid representation of the interaction potential that includes several repetitions of the primitive cell in the y direction.

As experimentally and theoretically studied in Refs. [35, 43], the collimation setup of the atomic beam governs

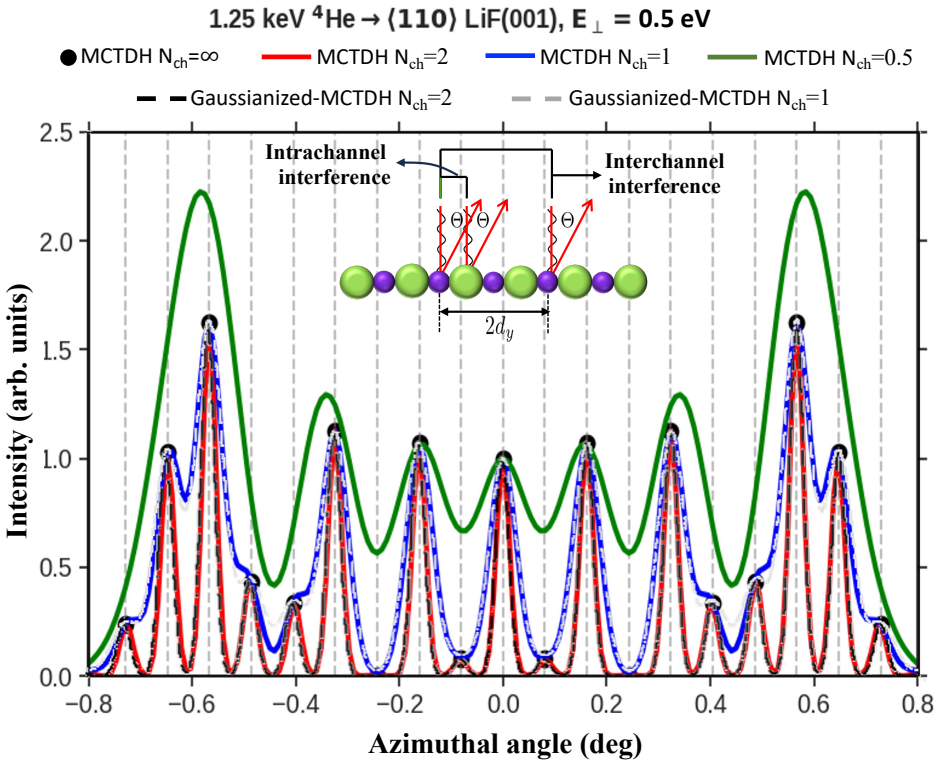

FIG. 1: (Color online) MCTDH spectra, as a function of the azimuthal angle φ_f, for different initial wave functions: Black circles display MCTDH results for $N_{ch} = +\infty$ [Eq. (6)], while solid lines show MCTDH results considering a finite transverse coherence length [Eq. (7)], with N_{ch} denoting the number of coherently illuminated channels, as given by Eq. (8). The dashed lines represent the spectra obtained from the Gaussianized-MCTDH method (see text for explanation). The vertical dashed lines indicate the positions $\varphi_f^{(B)}$ of the Bragg peaks. The inset depicts intrachannel and interchannel interference.

the transverse coherence length of the incident particles, which strongly affects the GIFAD patterns. For a given incidence condition, the σ_y value increases as the width of the collimation slit decreases [35, 60]. Current experimental setups have reduced this width to values smaller than 0.1 mm to increase σ_y, consequently lowering the beam divergence to less than 1 mrad [4, 39]. Throughout this work, the σ_y value will be expressed in terms of the number N_{ch} of equivalent axial channels that are coherently illuminated by the incident wave packet, which is defined as [60]:

$$N_{ch} = \frac{2\sigma_y}{d_y}, \tag{8}$$

where $d_y = 2.875$ Å is the width of the ⟨110⟩ channel of LiF(001). With this definition, we ensure that approximately 95% of the norm of the wave function is covering N_{ch} channels before projectile-surface collision. Notice that when $N_{ch} \to +\infty$ collimation effects banish and the final diffractogram will exhibit the delta-like diffraction peaks expected from *full* coherence MCTDH calculations.

Azimuthal MCTDH distributions derived from different initial wave functions are shown in Fig. 1 for ^{4}He impact with an incidence energy $E = K_i^2/(2m_P) = 1.25$ keV, where m_P is the projectile mass. The normal energy $E_\perp = E\sin^2\theta_i$, which controls the intrachannel interference, was chosen as $E_\perp = 0.5$ eV, corresponding to the intermediate range for He-LiF(001) GIFAD [30].

In Fig. 1, the azimuthal MCTDH spectra obtained by including a finite transverse coherence length, as given in Eq. (7), are compared with the Bragg intensities corresponding to the *full* coherence MCTDH distribution [Eq. (6)], which corresponds to $N_{ch} = +\infty$. As expected, the MCTDH distribution for $N_{ch} = 1$, which is associated with pure intrachannel interference, acts as an envelope function that determines the intensities of the delta-function peaks derived within the MCTDH method for $N_{ch} = +\infty$. But when the number of coherently illuminated channels increases becoming larger than 1, the MCTDH distribution displays a combination of intrachannel and interchannel interferences, as it is observed for $N_{ch} = 2$. In this case, the Bragg peaks are no longer delta functions, showing a finite width. However, their peak intensities agree with those of the *full* coherence calculation, being also modulated by the pure intrachannel distribution.

From Fig. 1, we can see that the shorter the transverse coherence length, the larger the width of the Bragg peaks.

Note however that the MCTDH spectrum for $N_{ch} = 0.5$ captures only partially the intrachannel interference and the curve does not match the intensities of all the *full* coherence peaks, as discussed in Ref. [38]. Therefore, we conclude that the use of Eq. (7) to describe the initial wave function allows one to simulate experimentally non-ideal collimating conditions.

In addition, in Fig. 1 we have included what we will hereafter call Gaussianized-MCTDH simulations. These latter results are obtained from the convolution of the *full* coherence MCTDH probability for a given Bragg order, with a Gaussian function with standard deviation $\sigma_{\rm G}$, so that the area of the Gaussian function matches the height of the corresponding MCTDH delta-function peak. In the Gaussianization used in Fig. 1, the width of the Gaussian functions was chosen to match that of the corresponding finite-coherence MCTDH spectra. But, generally speaking, this width can be chosen to account for the experimental resolution or to match the width of the peaks obtained within the SIVR approximation (see Sec. II C). At this point, it is also important to mention that, to make a meaningful comparison, the Gaussianized-MCTDH distribution must be normalized to one of the peaks of the spectrum with which we want to compare; for example, in Fig. 1 the central peak was normalized to that of the MCTDH spectrum for $N_{ch} = 2$. We observe that using this procedure, the Gaussianized curve for $N_{ch} = 2$ perfectly agrees with that obtained with the finite-coherence MCTDH method. A similar agreement is also found for $N_{ch} = 1$. But for $N_{ch} = 0.5$, the Gaussianized distribution slightly underestimates the intensity of the external peaks of the finite-coherence MCTDH spectrum. This fact might be associated with the influence of the spot-beam effect for $N_{ch} < 1$ [38].

C. Semiquantum simulations: SIVR approximation

The SIVR approximation is based on the IVR approach developed by Miller [44], which takes as a starting point the Feynman path integral formulation of quantum mechanics, introducing the standard Van Vleck approximation of the quantum time evolution operator [61, 62]. The resulting IVR time evolution operator is expressed in terms of classical trajectories with different initial conditions, without any additional assumptions (such as the widely employed stationary phase approximation), and allows for an approximate description of the classically prohibited transitions in terms of real value trajectories. The IVR method has been successfully applied to different atomic, molecular, and nuclear processes [63–67]. SIVR is an extension of IVR for addressing gas-surface scattering processes such as GIFAD. The SIVR approach makes use of the IVR time evolution operator of the quantum state of the projectile to derive a first-order time-dependent distorted wave theory. The interested reader can find details of its derivation in Refs. [33, 35].

Within the IVR method, it is possible to use different wave function bases to express the approximated time-evolution operator [44]. In particular, in previous articles [33, 35] the SIVR description of GIFAD was obtained by using a basis of Cartesian coordinates states $|\mathbf{R}\rangle$ of the projectile. But an equivalent approach can be derived by using a basis of coherent states $|\mathbf{p}, \mathbf{r}\rangle$, defined as [68]

$$\langle \mathbf{R}|\mathbf{p}, \mathbf{r}\rangle = \left(\frac{\gamma}{\pi}\right)^{3/4} \mathrm{e}^{-\frac{\gamma}{2}(\mathbf{R}-\mathbf{r})^2} \mathrm{e}^{i\mathbf{p}\cdot(\mathbf{R}-\mathbf{r})}, \tag{9}$$

with γ being a positive real parameter. The $|\mathbf{p}, \mathbf{r}\rangle$ states are Gaussian wave packets with fixed spatial and momentum dispersions, $\sigma_{\rm s} = (2/\gamma)^{1/2}$ and $\sigma_{\rm m} = (2\gamma)^{1/2}$, respectively [69]. Hence, they are hybrid states, intermediate between position and momentum eigenstates, which become position eigenstates $|\mathbf{r}\rangle$ as $\gamma \to +\infty$ and momentum eigenstates $|\mathbf{p}\rangle$ as $\gamma \to 0$.

By employing the coherent states of Eq. (9) within the IVR method [44], the scattering state of the projectile at the time t can be expressed as :

$$\begin{aligned} \left|\Psi_i^{(SIVR)}(t)\right\rangle \;=\; & \int d\mathbf{R} \int d\mathbf{R}_o \; f_s(\mathbf{R}_o) \int d\mathbf{P}_o \; f_m(\mathbf{P}_o) \\ & \times \frac{C(t)^{1/2}}{(2\sqrt{2}\pi)^3} \; \langle \mathbf{R}|\mathbf{P}_o, \mathbf{R}_o\rangle^* \; \Phi_i(\mathbf{R}) \\ & \times \; \exp(iS_t) \, |\mathbf{P}_t, \mathbf{R}_t\rangle \, , \end{aligned} \tag{10}$$

where the asterisk indicates the complex conjugation and

$$\Phi_i(\mathbf{R}) = \frac{1}{(2\pi)^{3/2}} \mathrm{e}^{i\mathbf{K}_i\cdot\mathbf{R}} \tag{11}$$

is the initial wave function of the projectile, with $\mathbf{R}$ the position vector of the center of mass of the incident atom and $\mathbf{K}_i$ the initial projectile momentum. In Eq. (10), the coherent state $|\mathbf{P}_t, \mathbf{R}_t\rangle$ is associated with the time-evolved position ($\mathbf{R}_t$) and momentum ($\mathbf{P}_t$) of the incident atom at a given time t, which are derived by considering a classical trajectory $\mathbf{R}_t \equiv \mathbf{R}_t(\mathbf{R}_o, \mathbf{P}_o)$ with starting ($t_o = 0$) position $\mathbf{R}_o$ and momentum $\mathbf{P}_o$. The momentum P_t is calculated from the classical trajectory as $\mathbf{P}_t = m_P d\mathbf{R}_t/dt$, while the functions $f_s(\mathbf{R}_o)$ and $f_m(\mathbf{P}_o)$, given respectively by Eqs. (12) and (14) of Ref. [35], describe the spatial and momentum profiles of the initial wave packet at a fixed distance Z_o from the surface, where the atomic projectile is hardly affected by the surface interaction. The function S_t denotes the classical action along the trajectory

$$S_t = \int_0^t dt' \; \left[\frac{\mathbf{P}_{t'}^2}{2m_P} - V_{PS}(\mathbf{R}_{t'})\right], \tag{12}$$

with V_{PS} the projectile-surface interaction, and the function

$$C(t) = \det\left[\frac{\partial \mathbf{R}_t}{\partial \mathbf{R}_o} + \frac{\partial \mathbf{P}_t}{\partial \mathbf{P}_o} + \frac{\gamma}{i}\frac{\partial \mathbf{R}_t}{\partial \mathbf{P}_o} + \frac{i}{\gamma}\frac{\partial \mathbf{P}_t}{\partial \mathbf{R}_o}\right] \quad (13)$$

is a determinant evaluated along the classical path.

We use the SIVR scattering state, given by Eq. (10), within the framework of the time-dependent distorted-wave formalism [70]. Following steps similar to those of Ref. [33], the SIVR amplitude for the transition $\mathbf{K}_i \rightarrow \mathbf{K}_f$ can be expressed as

$$A_{if}^{(SIVR)} = \int d\mathbf{R}_o\ f_s(\mathbf{R}_o) \int d\mathbf{P}_o\ f_m(\mathbf{P}_o) \times a^{(SIVR)}(\mathbf{R}_o, \mathbf{P}_o), \quad (14)$$

where

$$a^{(SIVR)}(\mathbf{R}_o, \mathbf{P}_o) = \frac{-i}{(2\pi)^6} \exp[-\frac{(\mathbf{K}_i - \mathbf{P}_o)^2}{2\gamma}] \times \int_0^{+\infty} dt\ C(t)^{1/2}\ G_{PS}(t) \times \exp\left[i\left(\varphi_t^{(SIVR)} - \mathbf{Q}\cdot\mathbf{R}_o\right)\right] \quad (15)$$

is the partial transition amplitude associated with the classical path $R_t(\mathbf{R}_o, \mathbf{P}_o)$ and $\mathbf{Q} = \mathbf{K}_f - \mathbf{K}_i$ is the projectile momentum transfer, with $\mathbf{K}_f$ being the final projectile momentum that satisfies $K_f = K_i$ (i.e., elastic scattering). The SIVR phase at the time t,

$$\varphi_t^{(SIVR)} = \int_0^t dt' \left[\frac{1}{2m_P}(\mathbf{K}_f - \mathbf{P}_{t'})^2 - V_{PS}(\mathbf{R}_{t'})\right], \quad (16)$$

coincides with that of the previous SIVR approach [33], while the function $G_{PS}(t)$ takes into account the 3D projectile-surface interaction along the trajectory,

$$G_{PS}(t) = \int d\mathbf{r}\ V_{PS}(\mathbf{R}_t + \mathbf{r}) \exp\left[-\frac{\gamma}{2}\mathbf{r}^2\right] \times \exp\left[-i\,(\mathbf{K}_f - \mathbf{P}_t)\cdot\mathbf{r}\right], \quad (17)$$

but averaging its contribution around the surroundings. An analytical expression of $G_{PS}(t)$ can be obtained by expanding such contribution to first order in $\mathbf{r}$, reading

$$G_{PS}(t) \simeq \left(\frac{2\pi}{\gamma}\right)^{3/2} \left[V_{PS}(\mathbf{R}_t) + \frac{i}{\gamma}\mathbf{F}_{PS}(\mathbf{R}_t)\cdot(\mathbf{K}_f - \mathbf{P}_t)\right] \times \exp\left[-(\mathbf{K}_f - \mathbf{P}_t)^2/(2\gamma)\right], \quad (18)$$

where $\mathbf{F}_{PS}(\mathbf{R}) = -\nabla_{\mathbf{R}} V_{PS}(\mathbf{R})$ denotes the force acting on the projectile at the $\mathbf{R}$ position. Note that, as expected, when $\gamma \rightarrow +\infty$ the partial transition amplitude $a^{(SIVR)}$ given by Eq. (15) tends to that given by Eq. (9) of Ref. [33], which will be here named as the SIVR coordinate form.

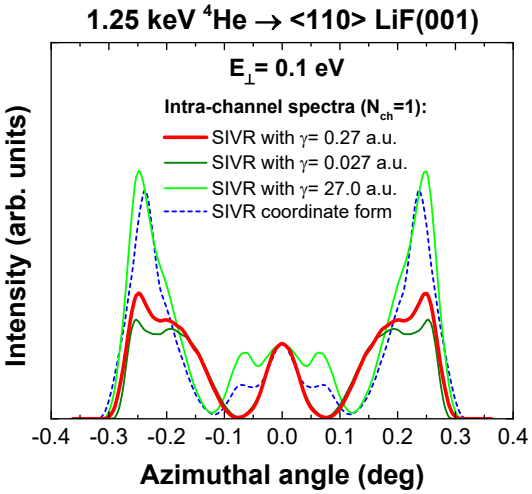

FIG. 2: (Color online) Intrachannel spectra, as a function of the azimuthal angle φ_f, for ^{4}He incidence with $E = 1.25$ keV and $E_\perp = 0.1$ eV. Solid lines, SIVR distributions derived from Eq. (19) for different γ values; blue dashed line, projectile distribution obtained by using the SIVR coordinate form, as given by Eq. (9) of Ref. [33].

The SIVR differential probability for elastic scattering with final momentum $\mathbf{K}_f$ in the direction of the solid angle $\Omega_f \equiv (\theta_f, \varphi_f)$ is obtained from Eq. (14) as

$$dP^{(SIVR)}/d\Omega_f = K_f^2 \left|A_{if}^{(SIVR)}\right|^2. \quad (19)$$

1. *Dependence on the parameter γ*

The SIVR partial amplitude $a^{(SIVR)}$ given by Eq. (15) depends on the parameter γ, which determines the features of the intermediate coherent states $|\mathbf{p}, \mathbf{r}\rangle$. Notice that the states $\{|\mathbf{p}, \mathbf{r}\rangle\}$ form an over-complete basis of quantum states [68]. However, as already reported for different applications of the IVR method [71–74], we find that the SIVR simulations are affected by the γ value. Therefore, in this subsection we analyze the influence of γ on the projectile distributions obtained within the SIVR approach.

Since the relative intensities of the diffraction maxima are determined by the intrachannel factor, associated with the interference inside a single channel, we confine our study of the γ-dependence to $N_{ch} = 1$ spectra for ^{4}He impact with $E = 1.25$ keV and different normal energies.

For a low energy case, $E_\perp = 0.1$ eV, in Fig. 2 we compare azimuthal intrachannel spectra derived within the SIVR approximation using different γ values - $\gamma = 27.0$, 0.27, and 0.027 a.u. - along with results obtained employ-

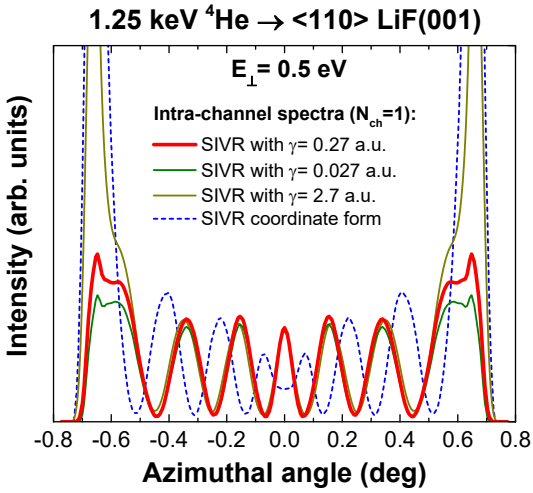

FIG. 3: (Color online) Analogous to Fig. 2 for $E_\perp = 0.5$ eV.

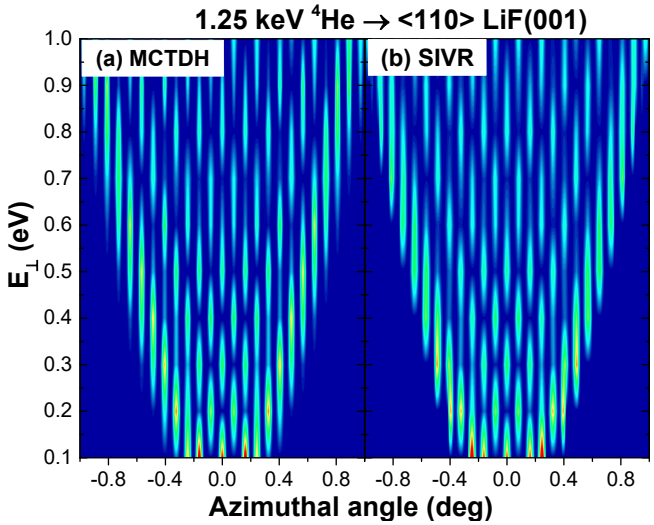

FIG. 4: Two-dimensional diffraction charts, in terms of the normal energy $E_\perp$ and the azimuthal angle φ_f, for ^{4}He impact along the $\langle 110\rangle$ channel with energy $E = 1.25$ keV. (a) Gaussianized-MCTDH results, with $\sigma_G = 0.01$ deg, and (b) SIVR simulations for $N_{ch} = 2$.

ing the SIVR coordinate form [33]. These γ parameters were chosen by taking as a reference $\gamma = 0.27$ a.u., a value for which the transverse length σ_y of the $|\mathbf{p}, \mathbf{r}\rangle$ states coincides with that of the coherently illuminated region (i.e., $\sigma_y = (2/\gamma)^{1/2} = N_{ch} d_y/2$, with $N_{ch} = 1$). For higher γ values, the spatial dispersion of the coherent states decreases, making the SIVR distribution gradually approximate to that derived from the coordinate form, as observed for the SIVR distribution with $\gamma = 27.0$ a.u. This latter SIVR distribution, as well as the one derived from the coordinate form, exhibit a broad structured peak at $\varphi_f = 0$ together with intense lateral maxima, which are associated with rainbow scattering. Note, in addition, that both the width of the central peak and the intensity of the outermost maxima diminish as γ decreases, and the SIVR distributions for $\gamma = 0.27$ a.u. and $\gamma = 0.027$ a.u. are very close to each other.

A similar γ-dependence of the azimuthal intrachannel distributions is observed in Fig. 3 for $E_\perp = 0.5$ eV. Using again the SIVR spectrum for $\gamma = 0.27$ a.u. as a reference, we find that the increase or decrease of this γ value by one order of magnitude almost does not affect the SIVR intrachannel spectrum, except for the outermost rainbow peaks, whose i intensity noticeably increases for $\gamma = 2.7$ a.u. Furthermore, the supernumerary maxima of these SIVR distributions are shifted about 0.07 deg with respect to those obtained within the SIVR coordinate form. Such φ_f shift of the supernumerary peaks is roughly independent on $E_\perp$ in the normal energy range from 0.2 to 1 eV.

From the analysis of the SIVR results displayed in Figs. 2 and 3, we will choose the γ value of the $|\mathbf{p}, \mathbf{r}\rangle$ intermediate states as the one that reproduces the transverse spatial width σ_y of the incident wave packet, whose spatial profile $f_s(\mathbf{R}_o)$ is included in Eq. (14). This choice will be thoroughly examined in Sec. III. A by contrasting the corresponding SIVR results with full quantum MCTDH distributions for different normal energies.

III. RESULTS

Our research focuses on He atoms impinging on a LiF(001) surface along the $\langle 110\rangle$ direction, with a normal energy $E_\perp$ ranging between 0.1 and 1.5 eV. Under these incidence conditions, the experimental projectile distributions present rich GIFAD patterns [30, 50]. In order to test the performance of the semiquantum approach, we compare SIVR simulations with pure quantum results derived from the MCTDH method, both calculations obtained by using not only the same PES, as given in Sec. II. A, but also the same transverse profile of the initial wave function (i.e., with the same finite transverse coherence length σ_y). The study is limited to a frozen ideal LiF surface, with the crystal atoms at rest at their equilibrium positions, that is, without including lattice vibrations (i.e., phonons). Furthermore, in all the cases SIVR results were derived from Eq. (14) choosing the γ value as $\gamma = 2/\sigma_y^2$, with σ_y the transverse width of the incident Gaussian wave packet, as discussed in Secs. II B.1 and II C.1.

A. Semiquantum vs. quantum methods

We start analyzing the overall features of the semiquantum distributions by contrasting SIVR and MCTDH diffraction charts for ^{4}He projectiles with an incidence energy $E = 1.25$ keV. Fig. 4 displays the SIVR two-dimensional chart, as a function of $E_\perp$ and φ_f, for an

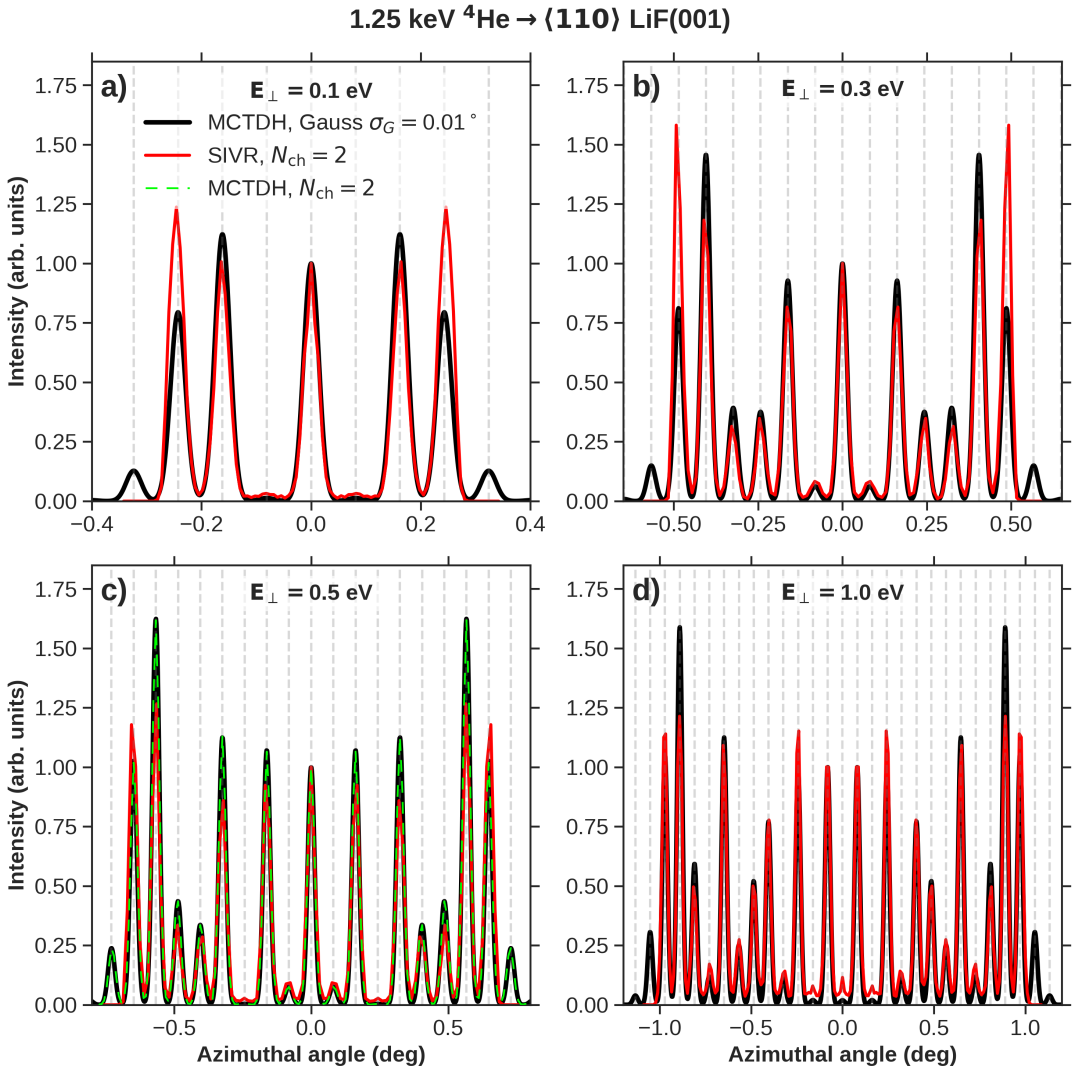

FIG. 5: Azimuthal projectile distributions, as a function of the azimuthal angle φ_f, for the case of Fig. 4 considering four different normal energies: (a) $E_\perp = 0.1$ eV, (b) $E_\perp = 0.3$ eV, (c) $E_\perp = 0.5$ eV, and (d) $E_\perp = 1$ eV. In all panels, the red solid line displays the SIVR distribution for $N_{ch} = 2$; black solid line, MCTDH distribution Gaussianized with $\sigma_G = 0.01$ deg, as explained in the text; green dashed line, MCTDH simulations with a finite transverse coherence length corresponding to $N_{ch} = 2$. The vertical dashed lines indicate the Bragg-peak positions.

initial wave packet involving $N_{ch} = 2$ channels coherently illuminated, together with the diffraction chart obtained from Gaussianized-MCTDH simulations. Both GIFAD charts were built from azimuthally projected distributions for different normal energies, normalized to their respective total intensities. Moreover, the transverse spatial width of the convolution function used in the Gaussianized-MCTDH calculations was fixed as $\sigma_G = 0.01$ deg to match the azimuthal width of the SIVR Bragg peaks (see Sec. II B.1). The computational cost of performing each of these calculations ranged from 96 h ($E_\perp = 0.1$ eV) to 42 h ($E_\perp = 1$ eV) of total CPU time in case of *full coherence* MCTDH (when 99.6% of the initial wave-packet is absorbed) and from 14 to 12 h in case of SIVR, measured in 2.6 GHz intel Xeon E5-2670 and 3.8 GHz intel i7 10700K processors, respectively. In appendix A we include a table with the computational resources required to complete a benchmark calculation ($E_\perp = 0.5$ eV) in more detail.

From Fig. 4, we observe that the SIVR chart is in good accord with the MCTDH one, reproducing very well the intensity modulation of the different Bragg orders as a function of $E_\perp$ along the whole normal energy range. But despite this remarkable agreement, it should be noticed that diffraction charts provide a qualitative, albeit extremely sensitive, description of the GIFAD patterns. Therefore, to thoroughly inspect the ability of the SIVR approach to reproduce full quantum GIFAD descriptions we should resort to the comparison of azimuthal projectile distributions.

In Fig. 5, we compare SIVR and MCTDH spectra, as a function of the final azimuthal angle φ_f, for different normal energies - $E_\perp = 0.1$, 0.3, 0.5, and 1.0 eV- under the incidence conditions of Fig. 4. That is, the SIVR results were obtained by considering $N_{ch} = 2$ axial channels coherently illuminated by the atomic beam [75], while the Gaussianized-MCTDH distributions were derived by convoluting the MCTDH probabilities for $N_{ch} = +\infty$ in order to fit the azimuthal width of the SIVR peaks. At this point, we stress that such convolution procedure was found to not only reproduce the MCTDH simulations for the corresponding finite transverse coherence length, as shown in Fig. 1, but also match the Bragg intensities of the *full* coherence MCTDH distribution. Furthermore, both SIVR and MCTDH spectra were normalized at the central peak (i.e., at $\varphi_f = 0$), except for Fig. 5 (d), where the central peak almost vanishes and the spectra were normalized at the first-order peaks.

From Fig. 5, we observe that the SIVR approximation describes the MCTDH azimuthal distributions for the different $E_\perp$ quite well. In particular, taking into account the extreme sensitivity of the GIFAD patterns, the remarkably good agreement between the suppressed or reduced-intensity Bragg orders of both spectra - SIVR and MCTDH - represents a clear indication of the reliability of the SIVR approach. However, note that in all the cases the azimuthal range of the SIVR distribution is slightly smaller than that of the MCTDH spectrum, partially missing the decreasing intensity of the Bragg peaks in the dark region of rainbow scattering. Moreover, for the lower normal energies [Figs. 5 (a) and 5 (b)], the outermost SIVR maxima are higher than those of the MCTDH distribution, due to an overestimation of the rainbow peak in the intrachannel factor. Both behaviors are related to the contribution of classically forbidden transitions in the outermost region of the rainbow peak. In this particular zone, the SIVR approach gives an approximate description of the involved quantum transitions, while the MCTDH method provides a full quantum treatment of them.

B. Experimental comparison

To investigate in more detail the performance of the SIVR and MCTDH methods under finite-coherence incidence conditions, in Fig. 6 we compare our theoretical results with an experimental spectrum of ^{4}He/LiF(001) GIFAD recently reported for a relatively high normal energy - $E_\perp = 1.45$ eV - [4], which displays rainbow and supernumerary rainbow maxima only. Hence, the SIVR distribution was evaluated considering a single-channel illumination (i.e., $N_{ch} = 1$), which corresponds to *pure* intrachannel interference. In Fig. 6, the intrachannel SIVR spectrum, as a function of the deflection angle $\Theta = \arctan(\varphi_f/\theta_f)$, is in good accord with the Gaussianized MCTDH distribution for $\sigma_G = 1.0$ deg, and both describe the angular positions of the experimental maxima

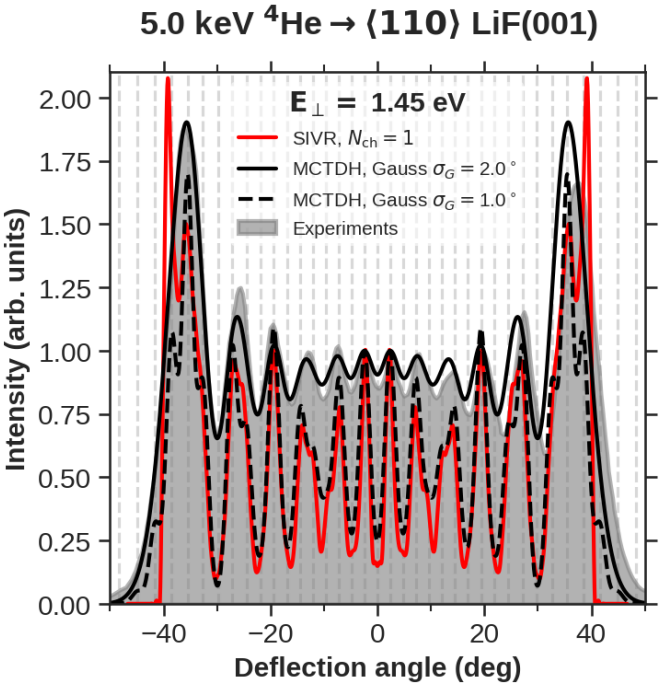

FIG. 6: Projectile distribution, as a function of the deflection angle Θ, for ^{4}He impact along the ⟨110⟩ channel with energy $E = 5$ keV and $E_\perp = 1.45$ eV. Experiments extracted from Fig. 17 of Ref. [4]. Simulations: red solid line, SIVR approximation for $N_{ch} = 1$; black dashed and solid lines, Gaussianized-MCTDH results with different σ_G values, as indicated. The vertical dashed lines indicate the Bragg-peak positions.

very well. Since the Θ positions of the supernumerary maximum are exceptionally sensitive to the corrugation of surface potential, this theoretical-experimental agreement reveals the adequate description provided by SIVR and MCTDH in combination with the PES model of Sec. II. A.

It is noteworthy that the experimental distribution of Fig. 6 presents a wide background, presumably due to the contribution of phonon-mediated processes, which are not included in our simulations. As mentioned in Sec. II. B. 1, GIFAD distributions are influenced by the collimation scheme, which determines the transverse coherence of the incident particles. But, in addition, at high normal energies the patterns become strongly affected by the phonon transitions, whose contribution introduces increasing decoherence as the normal energy augments [4, 76]. However, strikingly, if the *full* coherence MCTDH results are Gaussianized using $\sigma_G = 2.0$ deg to match the width of the experimental peaks, they are able to reproduce the relative intensities of the experimental spectrum. An analogous behavior can also be obtained by Gaussianizing the SIVR results. Alternatively, one can observe a moderate agreement with the experiments of Fig. 6 by adding a constant background to the theoretical distribution (See Appendix C, Fig. 9). At this

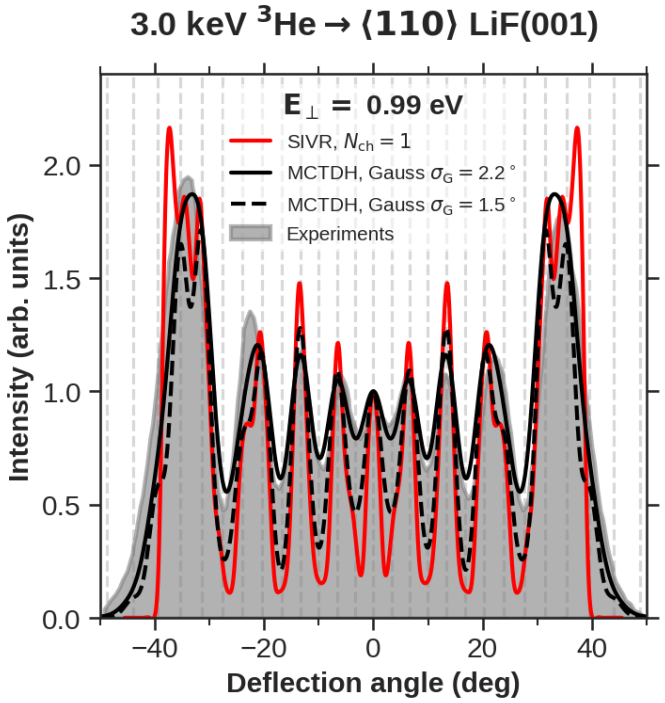

FIG. 7: Analogous to Fig. 6 for ^{3}He impact with energy $E = 3$ keV and $E_\perp = 0.99$ eV. Experiments extracted from Fig. 3 of Ref. [25].

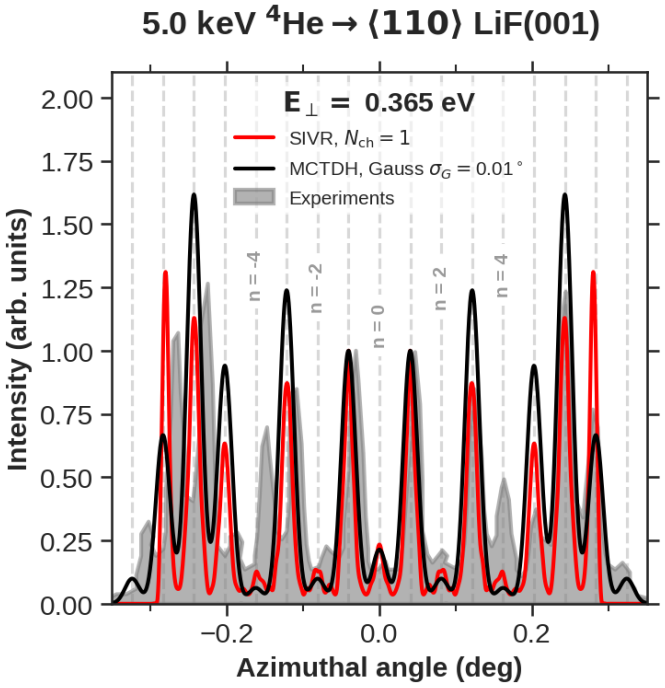

FIG. 8: Projectile distribution, as a function of the azimuthal angle, for ^{4}He impact along the ⟨110⟩ channel with energy $E = 5$ keV and $E_\perp = 0.365$ eV. Experiments extracted from Fig. 18 of Ref. [4]. Simulations: red solid line, SIVR approximation for $N_{ch} = 2$; black solid line, Gaussianized-MCTDH results with $\sigma_G = 0.01$ deg. The vertical dashed lines indicate the Bragg-peak positions.

point, we should stress that the precise relation between the widening of the peaks and/or the background cannot be derived from the present theoretical models, which are based on a static crystal. The contribution of inelastic phonon-mediated processes is indeed a topic that deserves further research [77].

In Fig. 7, we repeat the previous analysis by contrasting our simulations with experimental data for ^{3}He projectiles impinging on LiF(001) with $E_\perp = 0.99$ eV [25]. Again we observe that for $N_{ch} = 1$, the SIVR and Gaussianized-MCTDH (with $\sigma_G = 1.5$ deg) distributions agree with each other, accurately reproducing the angular positions of the experimental maxima. But, as in Fig. 6, the proper description of the experimental intensities with the Gaussianized-MCTDH method requires the increase of the Gaussian width to $\sigma_G = 2.2$ deg. The need of such a large convolution and/or a combination with a background (See Appendix C, Fig. 10) is still an open problem [76, 77].

Finally, in Fig. 8 the SIVR spectrum for $N_{ch} = 2$ along with Gaussianized-MCTDH results are compared with the experimental distribution for ^{4}He impact with $E_\perp = 0.365$ eV [4]. In this case, the SIVR and MCTDH simulations predict similar GIFAD patterns, with missing even-order peaks in the central region of the spectrum (i.e., for $n = 0$, ± 2, and ± 4). Such behavior is in agreement with the experimental data, except for $n = \pm 4$ where the experiment displays relatively intense maxima. Some factors that could be related to the mentioned differences observed between theory and experiment for this case could be the level of approximation of the PES description in this normal energy range and/or an experimental misalignment that produces a shift in the azimuthal positions of the Bragg peaks, which might affect their relative intensities. Furthermore, at this energy, the SIVR results overestimate the outermost-peak intensities of both the experimental and MCTDH distributions, as also seen in Fig. 5.

IV. CONCLUSIONS

Willing to further assess the suitability of the semi-quantum SIVR approach to reproduce, analyze, and extract information from GIFAD, we have performed a comparative study of SIVR with a full-quantum dynamics approach, namely, the MCTDH method. We have used He/LiF(001) as a benchmark system due to the amount of experimental measurements available in the literature. To ensure a detailed and accurate comparison, we have used the same He/LiF(001) PES, computed by applying the CRP procedure to a set of DFT energies, in both calculations. Moreover, we have taken into account the collimation effects in the MCTDH simulations, just as it is done in the SIVR ones, allowing us to scru-

tinize the influence of the initial wave-packet size. Our analysis reveals a remarkable agreement between SIVR and MCTDH diffraction charts and patterns. Theoretical simulations also show a very good accord with experimental measurements. Thus, from our assessment, we conclude that SIVR is a precise and versatile theoretical tool to study GIFAD-related phenomena.

Acknowledgments

The authors acknowledge financial support from MICINN (project PID2022-138288NB-C33) of Spain and from ANPCYT (projects PICT-2020-1755; PICT-2020-1434) and CONICET (project PIP 11220210100468CO) of Argentina. C.D. and A.S.M. acknowledge the generous allocation of computer time at CCC-UAM (Centro de Computación Científica, Universidad Autónoma de Madrid).

Appendix A: Computational resources

This section is not aimed to present a systematic comparison between MCTDH and SIVR computational resources usage. Calculations have been performed on different CPU architectures and chipsets and we only intend to show a qualitative view of the computing power required to simulate GIFAD spectra with both methods. To do so, we resume on table I the computational resources consumed by *full coherence* MCTDH ($N_{\rm ch} = \infty$), multi wave-packet MCTDH ($N_{\rm ch} = 2$) and SIVR calculations using the same initial condition. As stated in the main text, *full coherence* MCTDH computational resources were measured for calculations running in a 2.6 GHz intel Xeon E5-2670 processor, while SIVR resources were estimated in a 3.8 GHz intel i7 10700K processor. Computational resources used in multi wave-packet MCTDH calculations with $N_{\rm ch} = 2$ (see figure 1), were measured on a 3.0 GHz intel Xeon Gold 6248R processor. In MCTDH calculations, resources were monitored until 99.6% of the total wave-packet norm was absorbed by the complex absorbing potential located in the scattering channel

TABLE I: Computational resources required to run MCTDH ($N_{\rm ch} = \infty$), MCTDH ($N_{\rm ch} = 2$), and SIVR calculations for 1.25 keV ^{4}He, $\langle 110 \rangle$, and $E_\perp = 0.5$ eV initial conditions.

	MCTDH $N_{\rm ch} = \infty$	MCTDH $N_{\rm ch} = 2$	SIVR $N_{\rm ch} = 2$
total CPU time (h)	32	109	13
wall time (h)	3.5	25	13
number CPUS	16	16	1
RAM memory (MB)	40	1400	40
trajectories/wave-packets	1	19	2×10^5

Appendix B: Parameters used in MCTDH calculations

In Table 1, we list the parameters used in MCTDH simulations for He/LiF(001) GIFAD when *full* coherence (ideal perfect collimation) ($N_{\rm ch} = +\infty$) and finite coherence lengths ($N_{\rm ch} < +\infty$), respectively, are considered.

TABLE II: MCTDH parameters for quantum calculations with *full* coherence ($N_{\rm ch} = +\infty$) and finite coherence length ($N_{\rm ch} < +\infty$). $\Delta_{\rm RMS}$ and $\Delta_{\rm max}$ are the root mean square and maximum errors of POTFIT fit to the CRP potential used in SIVR calculations on the entire grid representation. When superscript (r) is present, it denotes that the error is measured only inside the dynamics relevant region. FFT stands for Fast Fourier Transform primitive basis set.

	Calculation type	
POTFIT grid parameters	$N_{\rm ch} = +\infty$	$N_{\rm ch} < +\infty$
X range (Å)	[0, 2.875]	[0, 2.875]
Y range (Å)	[0, 2.875]	[0, 25.875]
Z range (Å)	[0.2, 15.0]	[-2.0, 15.0]
Number of grid knots	72×72×324	36×324×324
Natural potential basis	15×15×contr	15×15×contr
Type of primitive basis	FFT	FFT
POTFIT accuracy	$N_{\rm ch} = +\infty$	$N_{\rm ch} < +\infty$
Relevant region	$V^{\rm 3D}$ <10 eV	$V^{\rm 3D}$ <10 eV
Iterations on rel. reg.	10	10
$\Delta_{\rm RMS}$, $\Delta^{(r)}_{\rm RMS}$ (meV)	0.76, 0.080	0.93, 0.11
$\Delta_{\rm max}$, $\Delta^{(r)}_{\rm max}$ (meV)	29, 2.2	29, 3.7
Complex absorbing potential	$N_{\rm ch} = +\infty$ and $N_{\rm ch} < +\infty$	
Z-range (Å)	[7.0, 15.0]	
order	2	
strength (au)	2.8×10^{-5}	
Initial wave function	$N_{\rm ch} = +\infty$	$N_{\rm ch} < +\infty$
Width, $\sigma_{\rm z}$ (Å)	2.0	2.0
Width, $\sigma_{\rm y}$ (Å)	$+\infty$	$\frac{N_{\rm ch} d_{\rm y}}{2}$
Z_0 position (Å)	10	10
Y_0 position (Å)	not defined	[11.50, 12.86]
num. wave packets	1	19
Dynamics parameters	$N_{\rm ch} = +\infty$ and $N_{\rm ch} < +\infty$	
SPFs x×y×z	10×15×20	
propagation time (fs)	[1000, 2000]	

Appendix C: Diffractograms with background addition

Although the proper description of the experimental distributions of Figs. 6 and 7 would require an adequate treatment of all the phonon-mediated processes, here we show how the SIVR distributions for $N_{ch} = 1$ compare with the experiments (and with wide-width Gaussianized MCTDH results) when a constant background is added to the SIVR probability.

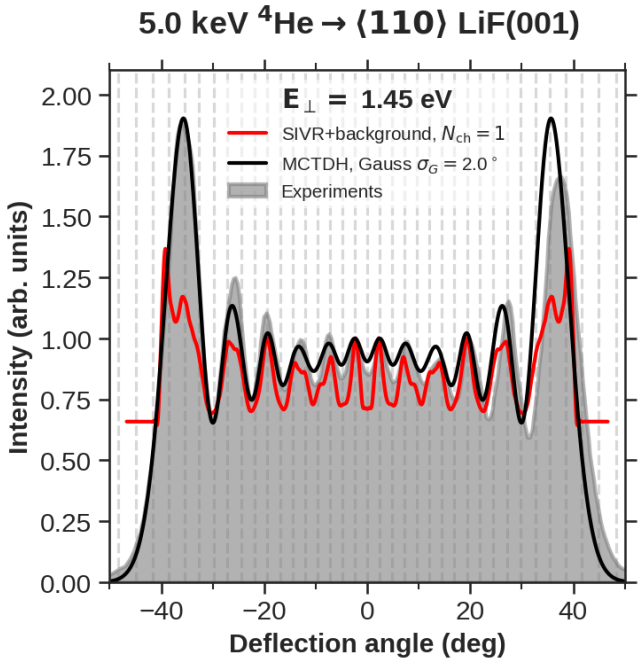

FIG. 9: Analogous to Fig. 6. Simulations: red solid line, SIVR approximation for $N_{ch} = 1$ with a constant background addition and; solid black line, Gaussianized-MCTDH with $\sigma_G = 2.0^\circ$.

[1] A. Schüller, S. Wethekam, and H. Winter. *Phys. Rev. Lett.*, 98:016103, 2007.
[2] P. Rousseau, H. Klemliche, A. G. Borisov, and P. Roncin. *Phys. Rev. Lett.*, 98:016104, 2007.
[3] H. Winter and A. Schüller. *Prog. Surf. Sci.*, 86:169–221, 2011.
[4] M. Debiossac, P. Pan, and P. Roncin. *Phys. Chem. Chem. Phys.*, 23:7615–7636, 2021.
[5] H. Hoinkes. *Rev. Mod. Phys.*, 52:933, 1980.
[6] D.R. Frankl. *Prog. Surf. Sci.*, 13:285, 1983.
[7] J. Barker and D. Auerbach. *Surf. Sci. Rep.*, 4:1, 1984.
[8] D. Farías and K.-H. Rieder. *Rep. Prog. Phys.*, 61:1575–1664, and references therein, 1998.
[9] J. Griesche, N. Hoffmann, M. Rabe, and K. Jacobs. *Prog. Cryst. Growth Charact. Mater.*, 37:103–121, 1998.
[10] H. Khemliche, P. Rousseau, P. Roncin, V. H. Etgens, and F. Finocchi. *Appl. Phys. Lett.*, 95:151901, 2009.
[11] C. Díaz and M. S. Gravielle. Grazing incidence fast atom and molecule diffraction: theoretical challenges. *Phys. Chem. Chem. Phys.*, 24:15628–15656, 2022.
[12] S. Lorenz, A. Gross, and M. Scheffler. *Chem. Phys. Lett.*, 395:210, 2004.
[13] B. Jiang and H. Guo. *J. Chem. Phys.*, 141:034109, 2014.
[14] X. J. Shen, Y. Xiao, W. Dong, X. H. Yan, and H. F. Busnengo. *Comput. Theor. Chem.*, 990:152, 2012.
[15] T. J. Frankcombe, C. M. Collins, and D. H. Zhang. *J. Chem. Phys.*, 137:144701, 2012.
[16] H. F. Busnengo, A. Salin, and W. Dong. *J. Chem. Phys.*, 112:7641, 2000.
[17] A. S. Muzas, F. Martín, and C. Díaz. *Nucl. Instr. Meth. Phys. Res. B*, 354:9–15, 2015.
[18] F. Aigner, N. Somonović, B. Solleder, L. Wirtz, and

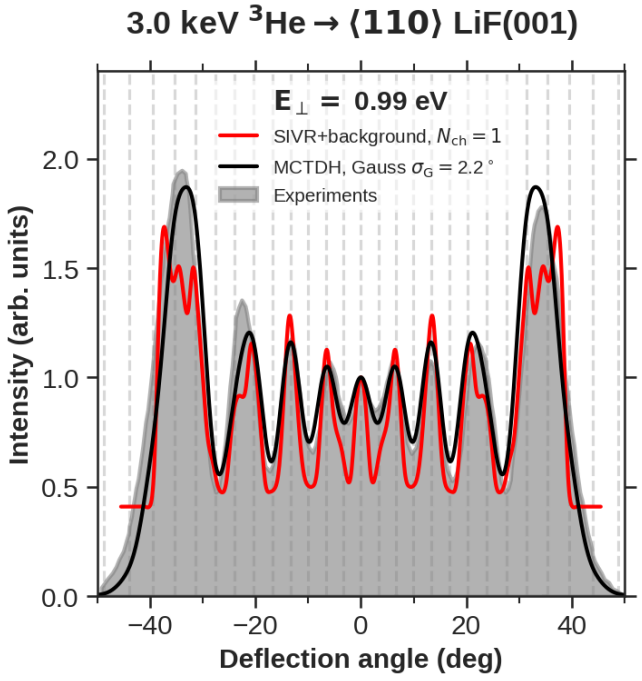

FIG. 10: Analogous to Fig. 7. Simulations: red solid line, SIVR approximation for $N_{ch} = 1$ with a constant background addition and; solid black line, Gaussianized-MCTDH with $\sigma_G = 2.2^\circ$.

J. Burgdörfer. *Phys. Rev. Lett.*, 101:253201, 2008.

[19] A. S. Muzas, F. Gatti, F. Martín, and C. Díaz. *Nucl. Instr. Meth. B*, 382:49–53, 2016.

[20] M. Debiossac, P. Roncin, and A. G. Borisov. *J. Phys. Chem. Lett.*, 11:4564–4569, 2020.

[21] E. A. Andreev. Quantum and Classical Characteristics of Glancing Scattering of Fast Atoms on the Surface of a Crystal. *Russ. J. Phys. Chem.*, 76:S164–S169, 2002.

[22] M. Busch, E. Meyer, K. Irmscher, Z. Galazka, K. Gärtner, and H. Winter. *Appl. Phys. Lett.*, 105:051603, 2014.

[23] A. Schüller, M. Busch, J. Seifert, S. Wethekam, H. Winter, and K. Gärtner. *Phys. Rev. B*, 79:235425, 2009.

[24] J. Seifert, A. Schüller, H. Winter, R. Wlodarczyk, J. Sauer, and M. Sierka. *Phys. Rev. B*, 82:035436, 2010.

[25] A. Schüller and H. Winter. *Phys. Rev. Lett.*, 100:097602, 2008.

[26] J. R. Manson, H. Khemliche, and P. Roncin. *Phys. Rev. B*, 78:155408, 2008.

[27] M. Debiossac, A. Zugarramurdi, H. Khemliche, P. Roncin, A. G. Borisov, A. Momeni, P. Atkinson, M. Eddrief, F. Finocchi, and V. H. Etgens. *Phys. Rev. B*, 90:155308, 2014.

[28] M. S. Gravielle and J. E. Miraglia. *Phys. Rev. A*, 78:022901, 2008.

[29] M. S. Gravielle and J. E. Miraglia. *Nucl. Instrum. Meth. Phys. Res. B*, 267:610–614, 2009.

[30] A. Schüller, H. Winter, M. S. Gravielle, J. M. Pruneda, and J. E. Miraglia. *Phys. Rev. A*, 80:062903, 2009.

[31] M. S. Gravielle, A. Schüller, H. Winter, and J. E. Miraglia. *Nucl. Instrum. Meth. Phys. Res. B*, 269:1208–1211, 2011.

[32] C. A. Ríos Rubiano, G. A. Bocan, M. S. Gravielle, N. Bundaleski, H. Khemliche, and P. Rocin. *Phys. Rev. A*, 87:012903, 2013.

[33] M. S. Gravielle and J. E. Miraglia. *Phys. Rev. A*, 90:052718, 2014.

[34] L. Frisco and M. S. Gravielle. *Phys. Rev. A*, 100:062703, 2019.

[35] M. S. Gravielle and J. E. Miraglia. *Phys. Rev. A*, 92:062709, 2015.

[36] G. A. Bocan, J. D. Fuhr, and M. S. Gravielle. *Phys. Rev. A*, 94:022711, 2016.

[37] G. A. Bocan and M. S. Gravielle. *Nucl. Instrum. Meth. Phys. Res. B*, 421:1–6, 2018.

[38] L. Frisco, J. E. Miraglia, and M. S. Gravielle. Spot-beam effect in grazing atom-surface collisions: From quantum to classical. *J. Phys.: Condens. Matter*, 30:405001, 2018.

[39] G. A. Bocan, H. Breiss, S. Szilasi, A. Momeni, E. M. Staicu Casagrande, M. S. Gravielle, E. A. Sánchez, and H. Khemliche. *Phys. Rev. Lett.*, 125:096101, 2020.

[40] G. A. Bocan, H. Breiss, S. Szilasi, A. Momeni, E. M. Staicu Casagrande, E. A. Sánchez, M. S. Gravielle, and H. Khemliche. *Phys. Rev. B*, 104:235401, 2021.

[41] M. H. Beck, A. Jäckle, G. A. Worth, and H. D. Meyer. *Phys. Rev.*, 324:1, 2000.

[42] H. D. Meyer, F. Gatti, and G. A. Worth. Multidimensional quantum dynamics: Mctdh theory and applications. 2009.

[43] J. Seifert, J. Lienemann, A. Schüller, and H. Winter. Studies on coherence and decoherence in Fast Atom Diffraction. *Nucl. Instrum. Methods Phys. Res. B*, 350:99–105, 2015.

[44] W. H. Miller. The Semiclassical Initial Value Representation: A Potentially Practical Way for Adding Quantum Effects to Classical Molecular Dynamics Simulations. *J. Phys. Chem A*, 105:2942–2955, and references therein, 2001.

[45] P. Giannozzi, S. Baroni, N. Bonini, M. Calandra, R. Car, C. Cavazzoni, D. Ceresoli, G. L. Chiarotti, M. Cococcioni, I. Dabo, A. Dal Corso, S. Fabris, G. Fratesi, S. de Gironcoli, R. Gebauer, U. Gerstmann, C. Gougoussis, A. Kokalj, M. Lazzeri, L. Martin-Samos, N. Marzari, F. Mauri, R. Mazzarello, S. Paolini, A. Pasquarello, L. Paulatto, C. Sbraccia, S. Scandolo, G. Sclauzero, A. P. Seitsonen, A. Smogunov, P. Umari, and R. M. Wentzcovitch. QUANTUM ESPRESSO: A Modular and Open-Source Software Project for Quantum Simulations of Materials. *J. Phys.: Cond. Matt.*, 21:395502, 2009.

[46] G. Kreese and D. Joubert. From Ultrasoft Pseudopotentials to the Projector Augmented-Wave Method. *Phys. Rev. B*, 59:1758, 1999.

[47] He.pbe-kjpaw_psl.1.0.0.UPF, Li.pbe-spn-kjpaw_psl.1.0.0.UPF, and F.pbe-n-kjpaw_psl.1.0.0.UPF. *www.quantum-espresso.org*, 2014.

[48] J. P. Perdew, K. Burke, and M. Ernzerhof. *Phys. Rev. Lett.*, 77:3865, 1996.

[49] J. Vogt and H. Weiss. The structure of KBr(100) and LiF(100) single crystal surfaces: a tensor low energy electron diffraction analysis. *Surf. Sci.*, 501:203–213, 2002.

[50] A. Schüller, S. Wethekam, D. Blauth, H. Winter, F. Aigner, N. Simonović, B. Solleder, J. Burgdörfer, and L. Wirtz. *Phys. Rev. A*, 82:062902, 2010.

[51] H. D. Meyer and G. A. Worth. *Theor. Chem. Acc.*, 109:251, 2003.

[52] R. van Harrevelt and U. Manthe. *J. Chem. Phys.*,

121:3829, 2004.
[53] C. Crespos, H. D. Meyer, R. C. Mowrey, and G. J. Kroes. *J. Chem. Phys.*, 124:074706, 2006.
[54] G. P. Krishnamohan, R. A. Olsen, G. J. Kroes, F. Gatti, and S. Woittequand. *J. Chem. Phys.*, 133:144308, 2010.
[55] M. del Cueto, A. S. Muzas, G. Füchsel, F. Gatti, F. Martín, and C. Díaz. *Phys. Rev. B*, 93:060301, 2016.
[56] M. del Cueto, A. S. Muzas, F. Martín, and C. Díaz. *Nucl. Instrum. Meth. Phys. Res. B*, 476:1–9, 2020.
[57] A. Jäckle and H. D. Meyer. *J. Chem. Phys.*, 104:7974, 1996.
[58] A. Jäckle and H. D. Meyer. *J. Chem. Phys.*, 109:3772, 1998.
[59] G.A. Worth, M.H. Beck, A. Jckle, H.D Meyer, Version 8.4 (2007) Seehttp://mctdh.uni-hd.de/, University of Heidelberg, Germany.
[60] M. S. Gravielle, J. E. Miraglia, and L. Frisco. Coherence-Length Effects in Fast Atom Diffraction at Grazing Incidence. *Atoms*, 6:64, 2018.
[61] J. V. Van Vleck. *Proc. Nat. Acad. Sci. USA*, 14:178, 1928.
[62] D. J. Tannor. *Introduction to Quantum Mechanics: A Time-Dependent Perspective*, chapter 10. University Science Books, Sausalito, 2007.
[63] D. E. Skinner and W. H. Miller. *Chem. Phys. Lett.*, 300:20, 1999.
[64] M. Thoss, H. Wang, and W. H. Miller. Generalized forward-backward initial value representation for the calculation of correlation functions in complex systems. *J. Chem. Phys.*, 114:9220–9234, 2001.
[65] C. H. Dasso, M. I. Gallardo, and M. Saraceno. Semiclassical calculation of heavy-ion scattering in the chaotic regime. *Phys. Rev. C*, 75:054611, 2007.
[66] W. H. Miller. Including quantum effects in the dynamics of complex (i.e., large) molecular systems. *J. Chem. Phys.*, 125:132305, 2006.
[67] N. Ananth, C. Venkataraman, and W. H. Miller. Semiclassical description of electronically nonadiabatic dynamics via the initial value representation. *J. Chem. Phys.*, 127:084114, 2007.
[68] M. F. Herman and E. Kluk. A semiclassical justification for the use of non-spreading wavepackets in dynamics calculations. *Chem. Phys.*, 91:27–34, 1984.
[69] C. Cohen-Tannoudji, B. Diu, and F. Laloë. *Quantum Mechanics*, chapter Comp. G_I. Willey-VCH, Paris, 2011.
[70] D. P. Dewangan and J. Eichler. Charge exchange in energetic ion-atom collisions. *Phys. Rep.*, 247:59–219, 1994.
[71] E. Kluk, M. F. Herman, and H. L. Davis. Comparison of the propagation of semiclassical frozen Gaussian wave functions with quantum propagation for a highly excited anharmonic oscillator. *J. Chem. Phys.*, 84:326–334, 1986.
[72] K. G. Kay. Numerical study of semiclassical initial value methods for dynamics. *J. Chem. Phys.*, 100:4432–4445, 1994.
[73] M. F. Herman. Improving the accuracy of semiclassical wavepacket propagation using integral conditioning techniques. *Chem. Phys. Lett.*, 275:445–452, 1997.
[74] S. Zhang and E. Pollak. Optimization of the semiclassical initial value representation of the exact quantum-mechanical real time propagator. *J. Chem. Phys.*, 119:11058–11063, 2003.
[75] The azimuthal SIVR spectra were calculated by integrating Eq. (19) over a tiny θ_f range centered on the Laue circle and with a central thickness 0.03 deg [78].
[76] L. Frisco and M. S. Gravielle. Decoherent phonon effects in fast atom-surface scattering. *Nucl. Instrum. Meth. Phys. Res. B*, 540:1–6, 2023.
[77] P. Pan, C. Kanitz, M. Debiossac, A. Le-Guen, J. Najafi Rad, and P. Roncin. Lateral line profiles in fast-atom diffraction at surfaces. *Phys. Rev. B*, 108:035413, 2023.
[78] M. Debiossac and P. Roncin. Image processing for grazing incidence fast atom diffraction. *Nucl. Instr. Methods Phys. Res. B*, 382:36–41, 2016.